Local wear resistance of Inconel 625 coatings processed by different thermal techniques: A comparative study

Rocío Cortés [a], Miguel Ángel Garrido-Maneiro [a,*], Heli Koivuluoto [b], Giovanni Bolelli [c], Stefania Morelli [c], Veronica Testa [c], Luca Lusvarghi [c], Jan Kondas [d], Pedro Poza [a]

[a] DIMME – Durability and Mechanical Integrity of Structural Materials, Escuela Superior de Ciencias Experimentales y Tecnología, Universidad Rey Juan Carlos, c/ Tulipán s/n, 28933 Móstoles, Madrid, Spain.
[b] Materials Science and Environmental Engineering, Faculty of Engineering and Natural Sciences, Tampere University, Korkeakoulunkatu 6, 33720 Tampere, Finland
[c] Department of Engineering "Enzo Ferrari", Università di Modena e Reggio Emilia, Via Pietro Vivarelli 10/1, 41125 Modena (MO), Italy
[d] Impact Innovations, Haun/Rattenkirchen, Germany

ARTICLE INFO

ABSTRACT

Ni-base superalloys, like Inconel 625, are extensively used in several applications due to their good performance at high temperature and their corrosion resistance. The high costs of these alloys promote their usage as coatings deposited onto cheaper materials. This practice improves the component performance without an excessive increment in price. Cold Spray (CS) deposition is a relatively new technology that could be considered as a real solid-state coating processing method. Consequently, no oxides are formed during CS deposition and the coatings do not lose their potential oxidation resistance. However, mechanical and tribological behaviour of CS materials is highly dependent on the processing parameters and powder feedstock properties. For these reasons, the aim of this work is to evaluate the mechanical properties and the local wear behaviour of high-pressure CS Inconel 625 coatings deposited under different spraying conditions by using different particle size distributions of powders. Nanoindentation tests were carried out on the coatings with a diamond Berkovich tip which determined the elastic modulus and hardness. Additionally, microscratch tests were also conducted to compute the local wear rate through the estimation of the removed volume. The cross profile of the residual grooves was recorded using the same tip as the one used to make scratch tests. These measurements were checked by Atomic Force Microscopy (AFM) analysis. The values obtained by both techniques were similar in the validation tests. The local wear rates were correlated with the mechanical properties and the scratch micromechanisms which were analysed in the scanning electron microscope. Finally, the results obtained were compared with those corresponding to coatings processed by more traditional methods.

1. Introduction

Ni-base superalloys are extensively used in different industrial sectors, like petrochemical [1,2], power generation [3,4], or aeronautical ones [5], due to their good performance at high temperature and their corrosion resistance. Inconel 625 is mainly a Ni–Cr–Mo alloy with some additional alloying elements, like Nb and Fe, which has been used in several applications for its excellent fabricability, high strength, and performance in aggressive environments. Inconel 625 can operate from cryogenic temperatures up to 982 °C. This is the primary reason for its acceptance in the chemical processing field. The aeronautical sector has chosen this material due to its high tensile, creep, and rupture strength which make it an interesting choice for aerospace applications [1,3,5].

Ni-base superalloys are reserved only to special components due to their high cost, compared to stainless steels. Consequently, these alloys are used when stainless steels are not suitable or when safety is critical [6]. For these reasons, the use of Ni-base superalloys as coatings to protect cheaper materials is a strategy to reduce costs whilst improving the components' behaviour. However, losses in performance could be observed, compared to bulk alloys, depending on the coating's processing [7].

Traditionally, Inconel 625 coatings have been deposited by laser cladding (LC) [8,9] and high temperature thermal spraying techniques, such as atmospheric plasma spraying (APS) [10], wire arc spraying

---

(ARC) [11] or high velocity oxy-fuel (HVOF) [12]. However, these processing routes involve high temperatures which could promote the formation of several oxides during deposition. Oxide formation reduces the corrosion resistance of the coating and leads to its embrittlement [13], decreasing the mechanical performance. Cold gas dynamic spray (CGDS), or simply cold spray (CS), deposition is a relatively new technology that can be considered as a real solid-state coating processing method. CS or kinetic deposition was discovered at the Institute of Theoretical and Applied Mechanics at Novosibirsk, Russia, in the middle of the 80s [14]. This technology is a high-rate materials deposition process, in which micrometric powder particles are accelerated to the substrate by a compressed gas jet at temperatures below their melting point [14–16], acquiring supersonic velocities in the range of 500–1200 m/s [15].

Consequently, no oxides are formed during CS deposition and the coatings do not lose their potential oxidation and corrosion resistance. Upon impact with the substrate, the kinetic energy of the particles is converted into severe plastic deformation and thermal energy, which disrupts the thin surface oxide films that are present on both parts. This allows intimate conformal contact between the surfaces under high local pressure, permitting bonding to occur by mechanical interlocking [17,18]. The successive accumulation of powder particles, plastically deformed and bonded together, builds up the coating. The characteristic solid-state condition of the deposition process promotes no phase transformations during cold spraying and lower tensile residual stresses in the coatings, compared with other thermal spraying techniques such as: plasma, flame, detonation and HVOF spraying [19,20].

CS is able to deposit coatings with thickness >1 mm. This is particularly interesting to establish maintenance and overhaul protocols to repair damaged components filling up the scraped parts by CS [21–23]. Conversely, the cold sprayed coating's performance is highly dependent on processing parameters like standoff distance, gas temperature or pressure, and also on powder particles characteristics, like size and shape. For the deposition of the powder to occur on the substrate, it must exceed a certain speed defined as critical velocity [19]. Schmidt et al. [24] carried out a study of the impact of a particle of 25 μm in diameter for a working temperature of 20 °C. These authors were able to predict the deposition window of Inconel 625, showing a critical velocity of 700 m/s and an erosion velocity of 1750 m/s from which an erosion process occurs, thus leading to the removal of material.

Assadi et al. [25] theoretically evaluated the parameter selection for CS obtaining results in agreement with Pontarollo et al. [26]. They established that the coatings produced with feedstock particles of larger dimensions showed lower porosity levels than those obtained from finer ones. A similar result was reported by Cavaliere et al. [27]. However, Chaudhuri et al. [28] studied the microstructural evolution of Inconel 625 superalloy coatings deposited by CS on a 4130 chrome alloy steel with medium carbon content. They reported successfully cold sprayed coatings without any oxidation using a powder with a size ranging between 5 μm and 25 μm. Wu et al. [29] also successfully cold sprayed Inconel 625 coatings on Al 6061 substrates. In this work, commercially available Inconel 625 powder with the particle size ranging from 10 μm to 70 μm was used as the feedstock in the cold spray deposition process. Therefore, it appears that there is no clear optimal size of the particles for spraying Inconel 625 coatings. In fact, other parameters, like the nozzle design or the gas pressure, affect the optimal powder size.

Additionally, Ni base superalloy components are used in aeronautical and power generation engines [30]. These components can be damaged by the impact of hard particles. These particles can be gravel or sand, and when impacting on the surface, they produce small craters which can lead to failures due to cracking [31]. Consequently, the analysis of the hardness and wear behaviour of Inconel 625 coatings is mandatory if they are to be used to repair damaged components. Shakil et al. [32] reported a microhardness value of 2.3 GPa for the bulk Inconel 625 alloy. This increment in the hardness value of the CS coatings is commonly explained by the strain hardening developed during the spraying process [29].

Hardness and wear resistance are often related when the behaviour of ductile materials is studied. Usually, the increase in hardness results in the increase in wear resistance [33,34], unless the increased hardness comes at a cost of excessive brittleness. Therefore, the CS Inconel 625 coatings are expected to have better tribological performance than the bulk alloy. Wang et al. [35] carried out ball-on-disc tests onto bulk Inconel 625 using Si_3N_4 and GCr15 ball with 6 mm diameter and a normal load of 15 N. They reported values of the specific wear rates that ranged from $5 \cdot 10^{-5}$ to $7.5 \cdot 10^{-5}$ $mm^3 \cdot N^{-1} \cdot m^{-1}$ at room temperature. The comparison of these values with those reported for the bulk material reveals that the wear behaviour of the coatings strongly depends on the test conditions and the behaviour of the material in the contact zone. Tribochemical phenomena, such as the generation of mechanically mixed layers or the formation of oxides, can also affect the wear behaviour, especially in continuous sliding tests. These tribolayers are developed during the wear tests and are formed by a mixture of oxides and metallic particles, which could come from both sides in contact. This subsurface layer is typically very fine-grained and could form a dense coherent layer on the wear surface, usually very smooth, or could be formed by a mixture of particles with similarities to mechanically alloyed materials. Their effect may be diminished if alternative tests such as one-way microscratches at the microscale are performed. Consequently, these tests could provide information about the mechanical integrity of these coatings, with less influence from tribochemical effects. Finally, the question arises of how much better are Inconel 625 coatings that are processed by CS in comparison to those obtained by other thermal spray techniques.

The study of the wear behaviour of Inconel 625 coatings has been mainly limited to analysis on a macroscopic scale. At this scale, it is not possible to discriminate the intrinsic wear resistance of the material from the effect of the defects generated by the spraying process. In this sense, microscratch tests allow an analysis of the wear resistance at local level. These tests may facilitate the identification of the intrinsic wear behaviour of the deposited material and the corresponding influence of the spraying parameters. Thus, the aim of this work is to use microscratch tests to evaluate the local wear behaviour of high-pressure CS Inconel 625 coatings deposited under different conditions by using powders with different particle size distributions. This study has been extended to Inconel 625 coatings processed by other thermal spraying techniques characterized by the melting of the deposited material.

2. Materials and methods

2.1. Feedstock powder and cold spray process

Inconel 625 (NiCr22Mo9Nb) coatings were deposited onto low carbon steels, S235JR structural steel substrates, using an ISS 5/11 CS system (Impact Innovations GmbH, Rattenkirchen, Germany) with a water-cooled OUT1/SiC nozzle. Previously, substrates were wiped with ethanol. Inconel 625 powders were provided by Sandvik Osprey (Neath, UK) and two size distributions were used: −25 + 5 μm (CS 1) and −38 + 15 μm (CS 2). Nominal chemical composition of Inconel 625 was 58 % (min) of Ni, ≤5 % of Fe, 20–23 % of Cr, 8–10 % of Mo, 3,15–4,5 % of Nb + Ta, ≤0,4 % of Al, ≤0,4 % of Ti, 3,15–4,15 % of Nb, ≤0,5 % of Mn, ≤0,5 % of Si, ≤0,015 of S and ≤1,0 % of Co, given by the supplier. Both powders were gas-atomized, having a spherical particle shape as can be seen in the Fig. 1. The two distributions fall into the category of fine and coarse powders, respectively [26].

Inconel 625 coatings were deposited using N_2 as propellant gas at the temperature of 1000 °C and a pressure of 5.5 MPa. This spraying temperature was selected because it was close to the melting temperature of the base material. The melting temperature for the Inconel 625 ranges between 1290 and 1350 °C [36]. Therefore, the CS spraying process occurred in the solid-state. Other parameters were a spray distance of 30 mm, a traverse speed of 500 mm/s, step of 1 mm, a powder feeding of
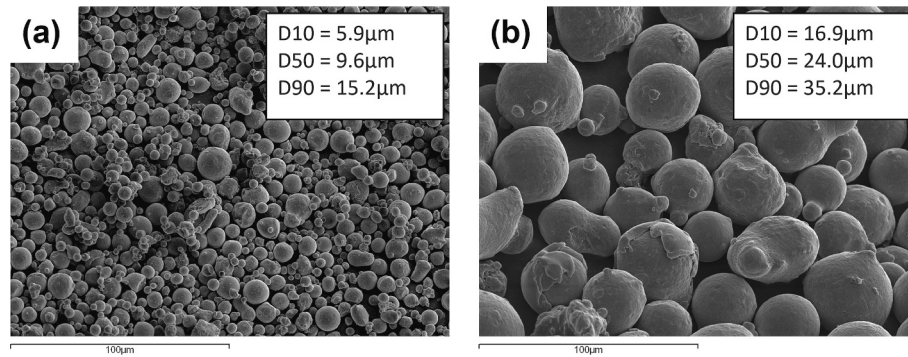
Fig. 1. a) Inconel 625 powder morphology provided by Sandvik Osprey (Neath, UK). b) Distributions of the different powders CS 1 and CS 2.

29.6 g/min and a layer amount of 4 layers. In addition, samples deposited by HVOF and ARC using the conditions presented previously by Fantozzi et al. [37] were also analysed. Finally, the results obtained were also compared with those presented by Verdi et al. [8,9] regarding the local microscratch resistance of LC Inconel 625. This will permit the comparison between the materials processed by CS and those deposited by more conventional, high temperature techniques.

2.2. Microstructure

Metallographic samples of the different studied materials were cut from the deposited coatings along the longitudinal cross section, parallel to the spraying direction and along the perpendicular one. The samples were ground using SiC papers up to 1200 grit and polished with a diamond slurry of up to 1 μm nominal size. After that, the surfaces were polished up to 0.5 μm using an alumina suspension. Subsequently, the polished surfaces were cleaned in deionized water and degreased in isopropyl alcohol. These samples were used to determine the hardness and the wear behaviour. Several samples were chemically etched using glyceregic reagent to reveal the microstructure. Two Scanning Electron Microscopes (SEM), a Zeiss ULTRAplus field-emission scanning electron microscope (Carl Zeiss AG, Oberkochen, Germany) and a Hitachi S3400 (Hitachi, Japan), were used to analyse the microstructure and the residual grooves of the microscratch tests. Both SEM were equipped with Energy Dispersive X-ray microanalysis (EDX). Secondary (SE) and Back Scattered Electron (BSE) images, with compositional contrast, were obtained.

2.3. Mechanical characterization

Vickers microhardness (H$_v$) tests were performed with a Buehler 2101 microhardness tester (Buehler, Esslingen, Germany) on the cross sections of the coatings. The samples were polished following the procedure described above. The tests were performed following the recommendations of the ISO 6507-1 standard [38]. Both a load of 100 gf and a dwell time of 12 s were used.

Additionally, nanoindentation tests (NHT, Anton Paar – Tritec, Corcelles, Switzerland) were carried out on the polished cross-sections of the CS coatings using a Berkovich indenter, whose area function was calibrated against a fuse silica standard. Load vs. penetration curves were recorded using a maximum load of 10 mN, a holding time of 15 s, and loading and unloading durations of 30 s (corresponding to linear loading and unloading rates of 20 mN/min). Matrices consisting of 6 rows of 40 indents each, aligned parallel to the coating/substrate interface direction, with a centre-centre spacing of 15 μm between adjacent indents, were performed around the mid-thickness location on the polished cross-sections, for a total of 240 indents on each sample. The indentation hardness (H$_{IT}$) and indentation modulus (E$_{IT}$) were extracted from the load vs. penetration curves using the Oliver-Pharr method according to the procedure laid out in the ISO 14577

standard. The results were expressed as mean ± standard deviation.

2.4. Tribological characterization

Following the tests arrangement selected in previous studies to evaluate the local wear behaviour of cold sprayed coatings [8,9,19], single local microscratch tests were carried out to estimate the wear resistance of the coatings. Both CS coatings were tested to evaluate the effect of feedstock powder size distribution on the local wear performance. Local microscratch tests were also performed onto the coatings processed by the others deposition techniques.

Local microscratch tests were performed onto the top surface of the polished coatings with a roughness Ra ~ 0,1 μm. Prior to the microscratch tests, the samples were cleaned in deionized water and degreased in isopropyl alcohol. A Nanoindenter G200 (Keysight Technologies Inc., Santa Rosa, CA, USA) was used to perform single direction microscratch tests following the procedure described in [8,9]. The nanoindenter was equipped with a Berkovich diamond indenter, with a tip radius of 20 nm, using the largest edge as a leading border. Fig. 2a) depicts a sketch of the experimental arrangement of the microscratch tests.

The microscratch length, L, used was 300 μm and the microscratch velocity was fixed at 10 μm s^{-1}. The load applied during the microscratch test, F_N, was 100 mN [8]. Five microscratch tests were performed on each sprayed coating. Each microscratch was separated from the adjacent ones by at least 60 μm. Four cross profiles were measured on each residual groove to determine the removed volume per microscratch length. Fig. 2b) shows an example of one of these cross profiles. They were characterized by two quasi-triangular geometries above the free surface of the coating. The third triangle area represents the displaced material which was characterized by the semi-angle α, that was consequence of the indenter passing through during the microscratching process. The semi-angle value (α) was evaluated through the cross profile generated onto the residual grooves when the microscratch tip ran perpendicular to the direction of the microscratch test itself.

The residual groove volume per unit of microscratch distance, V_d, was calculated using Eq. (1) [8]. This methodology and equation was previously validated with residual groove AFM analysis performed on Inconel 625 alloy coatings deposited by LC [8]. This wear parameter represents the volume that is displaced out of the scratch groove throughout the microscratch process. This volume is averaged over the scratch length. Part of it is just displaced plastically by ploughing into the lateral pile-ups. The remainder accumulates in front of the indenter until it is removed by cutting and/or cracking.

$$V_d = \frac{1}{L}\int_0^L tg\alpha\, h^2 dx = \frac{Total\ volume\ displaced}{Scratch\ length}\left(\frac{mm^3}{m}\right) \quad (1)$$

The dimensional local wear rate, k, was calculated from the V_d measurements through the Archard's equation [8]. The use of this volume is justified to obtain a wear rate even when all the displaced volume
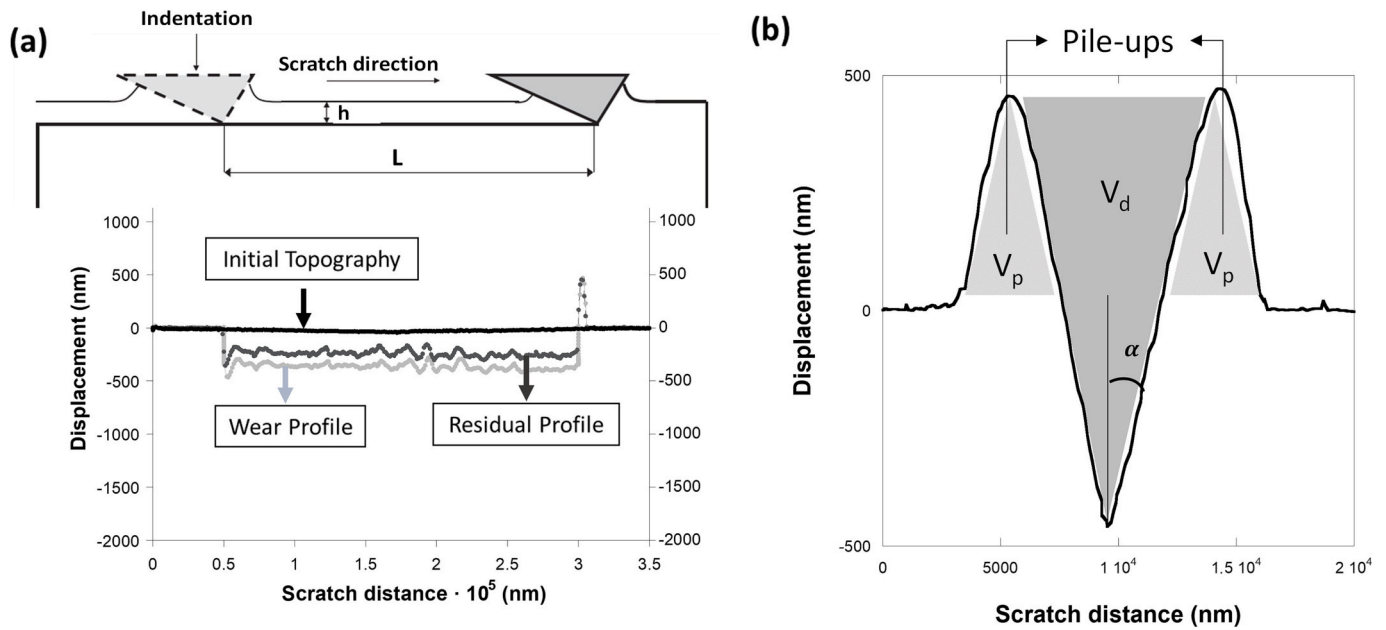
Fig. 2. a) Schematic display of the microscratch test arrangement. b) Representative microscratch cross profile (vertical axis is augmented to facilitate the identification of the details of the cross profile).

was accumulated at the residual edges due to plastic deformation.

$$k = \frac{V_d}{F_N} \left(\frac{mm^3}{N \cdot m} \right) \tag{2}$$

Fig. 2b) shows a representative cross profile of a residual scratch groove. The area that extends from the highest peak of the pile-ups to the deepest valley represents the material displaced in front of the indenter as a consequence of the indenter's movement until reaching the distance in which this cross profile was obtained. Consequently, this area represents the displaced volume per scratch length unit, V_d. Additionally, the areas corresponding to the pile-ups represent the volume per unit length of the material plastically displaced by ploughing, V_p. Consequently, the removed volume per unit of scratch distance, V_r, can be obtained as the difference between the displaced volume, V_d, and the volume accumulated by plastic deformation at the edges of the residual groove, V_p.

3. Results and discussion

3.1. Microstructure of the coatings

Fig. 3 shows representative cross sections of Inconel 625 coatings deposited by HVOF (Fig. 3a) and ARC (Fig. 3b). Fantozzi et al. [37]

analysed the microstructure of coatings processed using HVOF and ARC processes. Coatings deposited by HVOF showed Cr and Nb rich oxides located at the boundaries of the splats which were, instead, poorer in Ni. However, inside the splats the Ni content increased. In the case of ARC coatings, the main constituents of the oxides were Mo and Nb oxides. The main difference between the microstructure of the coatings processed by these techniques is that splats in the ARC coating were more flattened and fragmented than those in the coatings deposited by HVOF. Verdi et al. [8] observed a columnar dendritic microstructure in the LC coatings. A brighter secondary phase, enriched in Nb and Mo, was observed at the grain boundaries inside these LC coatings.

Table 1 presents the thickness measured on the different coatings: values corresponding to materials processed by HVOF, ARC and LC [8,37] are also included for comparison. These thickness values were measured on images like those shown in Fig. 4. The thickness values presented for the CS coatings, CS 1 and CS 2, suggest a correlation between thickness and particle size distribution. The smaller particles were accelerated at faster speeds [39], promoting higher cohesion between splats, and favouring a denser, hence thinner, coating [19,40].

The HVOF and ARC coatings were also dense, but the presence of different levels of greyscale contrast reveals the presence of significant amounts of oxide inclusions (Fig. 3). The HVOF coating, in particular, shows a non-uniform distribution of oxide inclusions (Fig. 3a), which
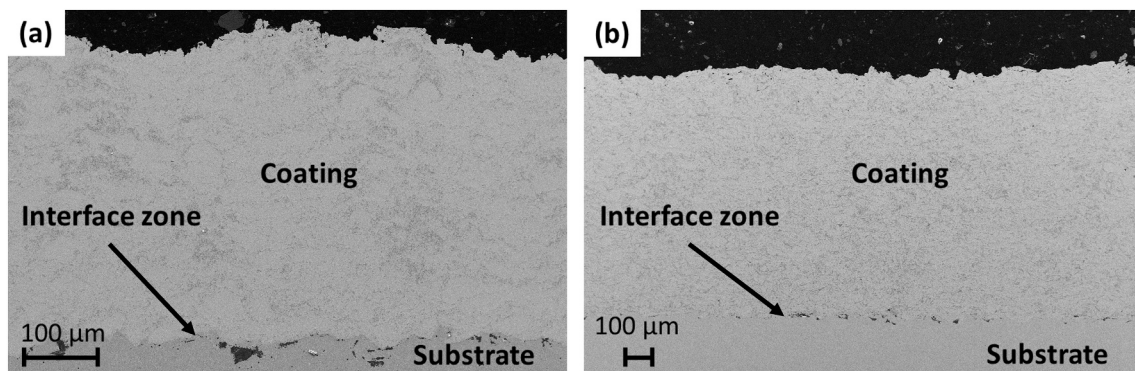

Fig. 3. Representative SEM SE images of the cross sections: a) HVOF coatings; b) ARC coatings.

Table 1
Thickness of the coatings processed by CS. The results corresponding to HVOF, ARC and LC are also included for comparison [8,37].

Coating	Spray system	Process gas	Feedstock material	Thickness (μm)
HVOF	Diamond Jet Hybrid 2700 (TUT)	Propane oxygen	−45 + 15 μm	406 ± 8
Arc Sprayed (ARC)	OSU Hessler	Air	Ø 1.6 mm	1010 ± 56
Laser Cladding (LC)	High-Power Diode Laser	Argon	−150 + 75 μm	1234 ± 58
Cold Spray 1 (CS 1)	Impact Innovations	N_2	−25 + 5 μm	407 ± 13
Cold Spray 2 (CS 2)	Impact Innovations	N_2	−38 + 15 μm	329 ± 26

may be due to the fine size of the feedstock powder (Table 1). Previous studies [41] have reported that the smallest particles may acquire a velocity component parallel to the substrate surface during the spraying process, increasing the interacting time with the stagnation flow. Additionally, the HVOF technique uses a highly oxidizing gas (Table 1). Both circumstances might promote the oxidizing process of the sprayed particles. However, the large molten droplets and the less oxidizing nature of the ARC technique (Table 1), could justify a lower oxidation of the particles regarding to the HVOF ones, as shown in Fig. 3.

Fig. 5 shows SE images from both CS coatings: the substrate-coating interface showed a good bonding with no signs of delamination. The coatings are formed by plastically deformed particles with very few pores located at the particles' boundaries. Indeed, it is often difficult to identify the exact boundaries between adjacent particles. Consequently, no oxides were observed, as it was expected in CS materials processed below the melting point [14,15].

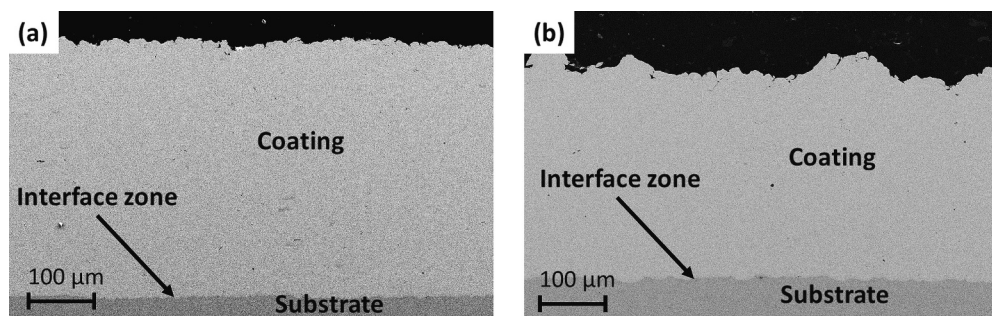Fig. 6 shows that the cold-spray particles developed strong solid-

Fig. 4. Representative SEM SE images of the cross sections of cold sprayed coatings: a) CS 1; b) CS 2.
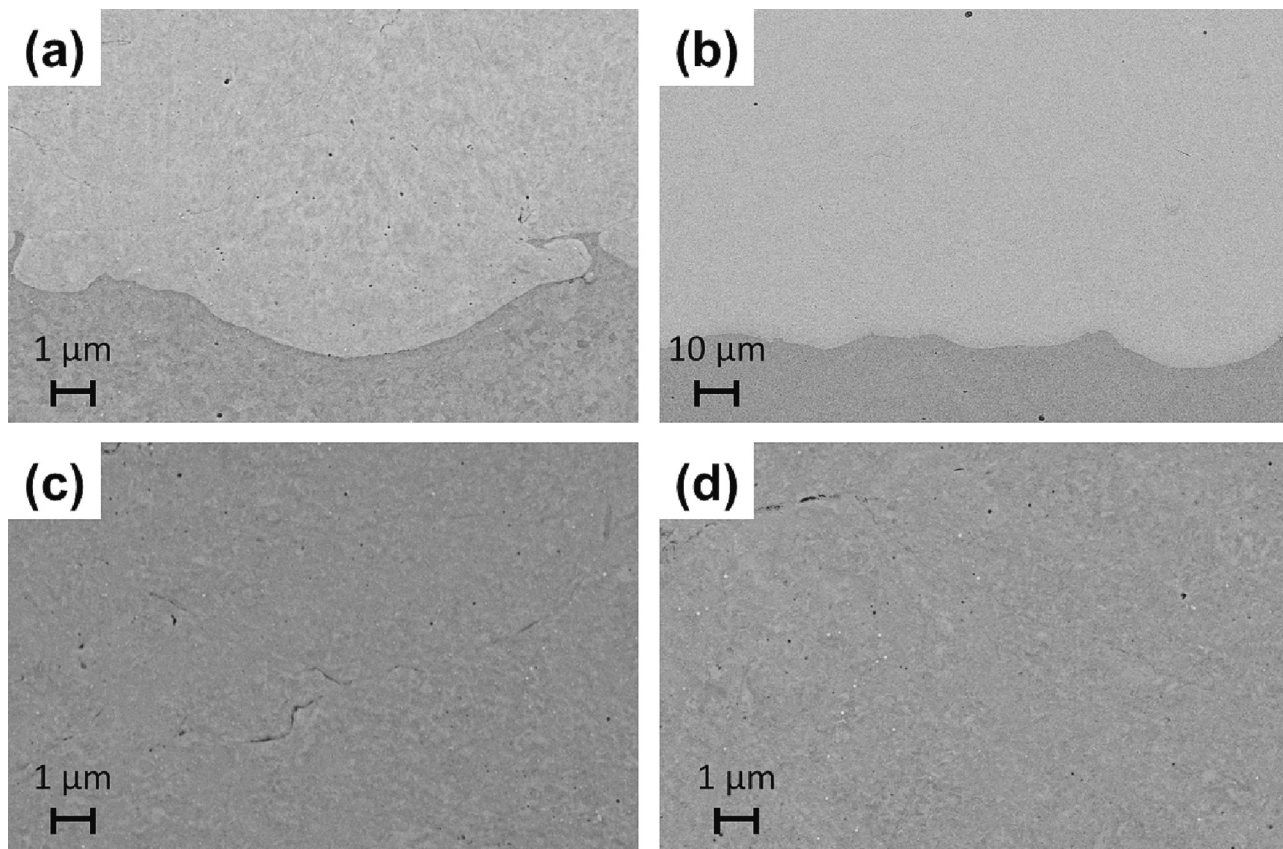

Fig. 5. SE images of cold sprayed Inconel 625 showing the coating-substrate interface and splats. a) and c) CS 1 (−25 + 5 μm). b) and d) CS 2 (−38 + 15 μm).
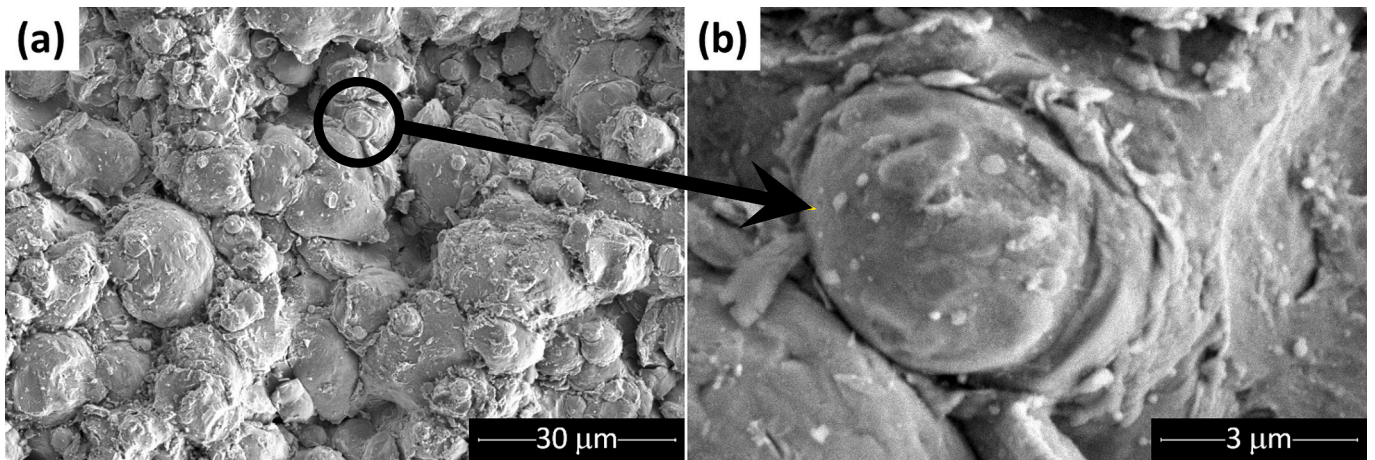
Fig. 6. SEM SE overview (a) of the top surface of CS Inconel 625, with detail (b) of jetting around a particle.

state bonding. The magnified view of panel (b) highlights the formation of jets around an impacted particle, which is the typical outcome of adiabatic shear instabilities at the particle/substrate interfaces, and particle/particle interfaces, as can be seen in Fig. 6. These features are usually associated with strong bonding at least along the periphery of the particle. The formation of such well-developed jets explains the tight interparticle bonding seen in Fig. 6. The jetting process could be observed at the substrate-coating interface of both CS coatings. Therefore, good adhesion was expected of them. Furthermore, no significant differences in the interface morphology (Fig. 5) were observed between both CS coatings. It appears that the particle sizes used in the spraying process of both coatings turned out to be suitable from the point of view
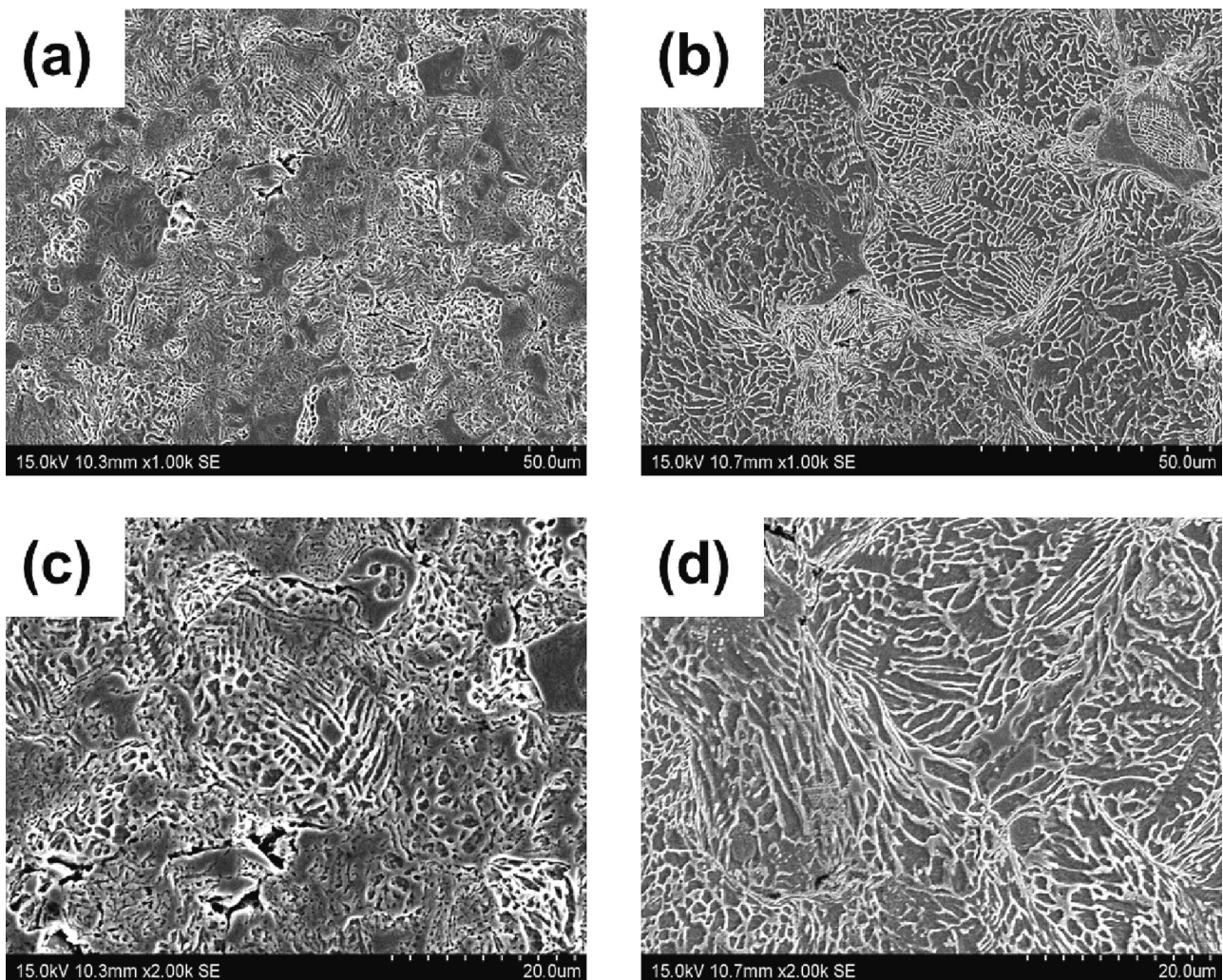

Fig. 7. SE images of etched cold sprayed Inconel 625 samples showing a dendritic microstructure. a) and c) CS 1 ($-25 + 5$ μm). b) and d) CS 2 ($-38 + 15$ μm).

of adhesion between the coating and the substrate. However, the effect of particle size on the adhesion between coating and substrate is not clear since it may also depend on the mechanical properties of the particles and the substrate. For example, Pontarollo et al. [26] deposited commercial Ni alloy (corresponding to the Inconel® 625 alloy) using feedstock powders of two different particle size distributions onto AISI316-L stainless steel by CS. In particular, Ni-alloy particles with size distributions of $-45 + 20$ μm (coarse powders) and $-20 + 5$ μm (fine powders) were sprayed. The gas used was nitrogen, the gas flow temperature and pressure ranged between 600 °C and 700 °C and 30–40 bar, respectively. The standoff distance was between 18 mm and 20 mm. They observed that fine powders gave a porous and low adherent coating with poor growth capability. On the contrary, a well adherent coating, with a porosity lower than 3 % and a dendritic microstructure, was obtained by using coarse powders. Conversely, Poirier et al. [42] deposited H13 chromium hot-work tool steel powders (tool steel) with particle size distributions nominally between 10 and 45 μm (coarse) and <16 μm (fine). They concluded that the smaller particles were beneficial for deposition rate and coating quality. However, when the coarse powder was used, the coatings´ microstructure exhibited poor adhesion.

To analyse the microstructure inside the splats, etched samples were observed by SEM. This analysis was carried out on the top surface. Fig. 7 shows that both CS 1 and CS 2 samples retain the dendritic microstructures of the gas-atomized feedstock powders, as could be expected for a fully solid-state deposition process. This dendrite structure was generated due to rapid cooling during the atomization process selected to produce the Inconel 625 particles [29]. Magnified views in panels Fig. 7c and d suggest that dendrites were plastically deformed to various extents across the impacted particles. The powder size distribution affects the dendrites size. The smaller particles possessed finer dendrites because of their higher cooling rate during the original gas-atomization process. Next to the particle boundaries, dendrites show particularly extensive plastic deformation, up to the point of being almost indistinguishable, as a result of the adiabatic shear instability and jetting phenomena previously shown in Fig. 6. This is especially clear in Fig. 7b, perhaps due to the interior of the coarser particles being less plastically deformed so the contrast with the highly deformed boundary is more apparent. Deformation, however, is more extensive throughout the finer particles (Fig. 7a), so the contrast between the interior and the boundary is visually less marked.

3.2. Mechanical properties

The mechanical properties were measured in the cross sections and carried out on a micro and nano scale. Fig. 8 shows the average and standard deviation of the microhardness values measured on the coatings processed by CS, HVOF and ARC. The value of microhardness of LC technique has been obtained by the reference [8]. The horizontal line represents the hardness value of 2.3 GPa for the bulk material [32]. The coatings deposited by CS exhibited higher values than those processed by conventional techniques. This tendency could be a consequence of the plastic deformation induced during the CS deposition process and can be observed in Fig. 7. If the sprayed material exhibits strain hardening, higher hardness values are to be expected in coatings deposited by CS. Indeed, Inconel 625 shows work hardening behaviour [38]. From the data supplied by the powder manufacturer, considering the Tabor relationship between hardness and yield strength, an approximate hardness value of 2.52 GPa could be obtained. Consequently, the tendency observed in Fig. 8 was expected. Wu et al. [29] sprayed Inconel 625 powder (10 μm to 70 μm) by CS. In this investigation, nitrogen (N$_2$) was used as the propellant gas, heated to 1000 °C and pressurized to 4.7 MPa. The nozzle was positioned perpendicular to the substrate surfaces with a standoff distance of 30 mm. The microhardness of the resulting coatings was 4.29 ± 0.43 GPa, 4.40 ± 0.37 GPa and 4.48 ± 0.53 GPa for indentation loads of 0.5 kgf, 0.3 kgf and 0.1 kgf, respectively. Although there is a certain trend in the values, the differences are not significant. Even so, these values are considerably larger than those reported for the bulk alloy. Borchers et al. [43] compared the deformation behaviour of 316L stainless steel powders in cold spraying and explosive powder compaction, subsequently correlating the observed microstructures with the respective energy inputs. They used gas atomised austenitic steel 316L powders with three different powder size distributions, <22 μm (fine), 15 to 45 μm (medium) and 53 to 177 μm (coarse). They reported an inversely proportional relation between particle size and hardness, therefore confirming that the greater the plastic deformation (which occurs with finer particles), the greater the hardness. This tendency can also be observed in Fig. 8 comparing the hardness of both CS coatings, which is also consistent with the observation that the interior of coarser particles was less plastically deformed (Fig. 7b). Nonetheless, the difference between the hardness values of the CS 1 and CS 2 coatings is rather small, compared with the associated standard deviations. In this respect, it is interesting to note that slightly higher statistical scatter was observed for the coatings sprayed with larger particles.
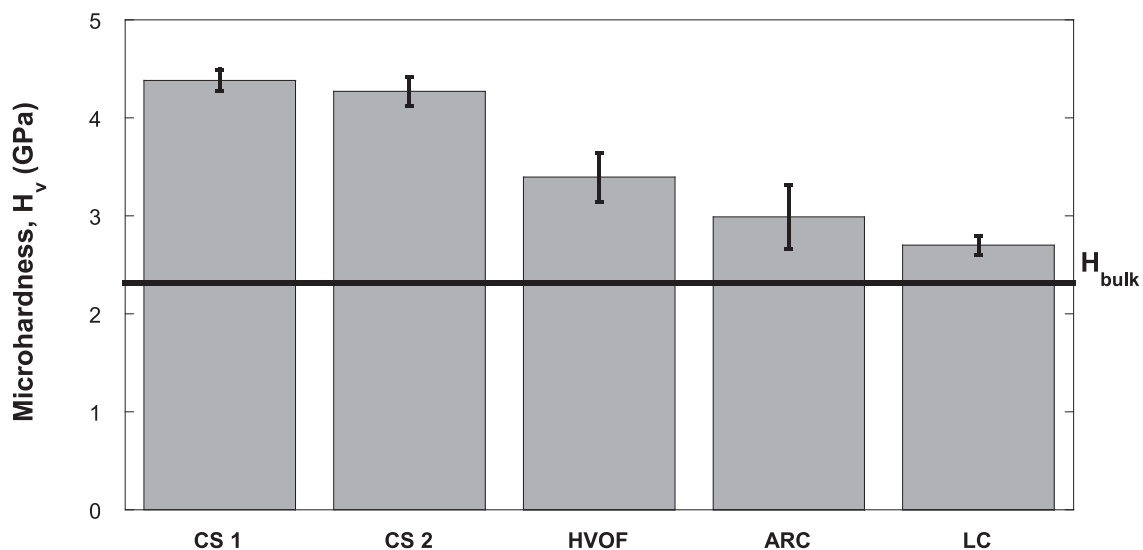

Fig. 8. Microhardness values of the coatings processed by different techniques. LC coatings microhardness value from [9].

Conversely, the lowest microhardness values were obtained for the coatings deposited by the ARC and LC processes. Yung et al. [44] measured the Vickers microhardness of Inconel 625 coatings deposited by wire ARC onto SS304L plates and reported an average value of 3.32 GPa. This value corresponds to that shown in Fig. 8 for the ARC technique. This hardness value, which was lower than the ones measured on CS and HVOF coatings, may be related to the poorer interlamellar cohesion since in-flight velocities in ARC spraying are lower than in CS and HVOF. In addition, the strain hardening which takes place during deposition is much lower in ARC sprayed and LC coatings due to the lower particles' velocity, compared with that observed in HVOF and, in a

major extent, in CS. The coarser lamellae and the presence of a relatively large fraction of oxides may also compromise the strength of the ARC coatings, justifying their lower hardness values [45]. However, the LC coating shows even lower hardness. This result may be related to the significant dilution identified in these coatings due to the high heat input during the deposition process [45]. Feng et al. [46] studied the Vickers microhardness and wear behaviour of Inconel 625 coatings fabricated by LC and shielded metal arc welding. Additionally, both properties were correlated to the coatings' microstructure. They observed a significant zone of the coating affected by the Fe-dilution process. This phenomenon affected the hardness of the coatings. Values between 2.4
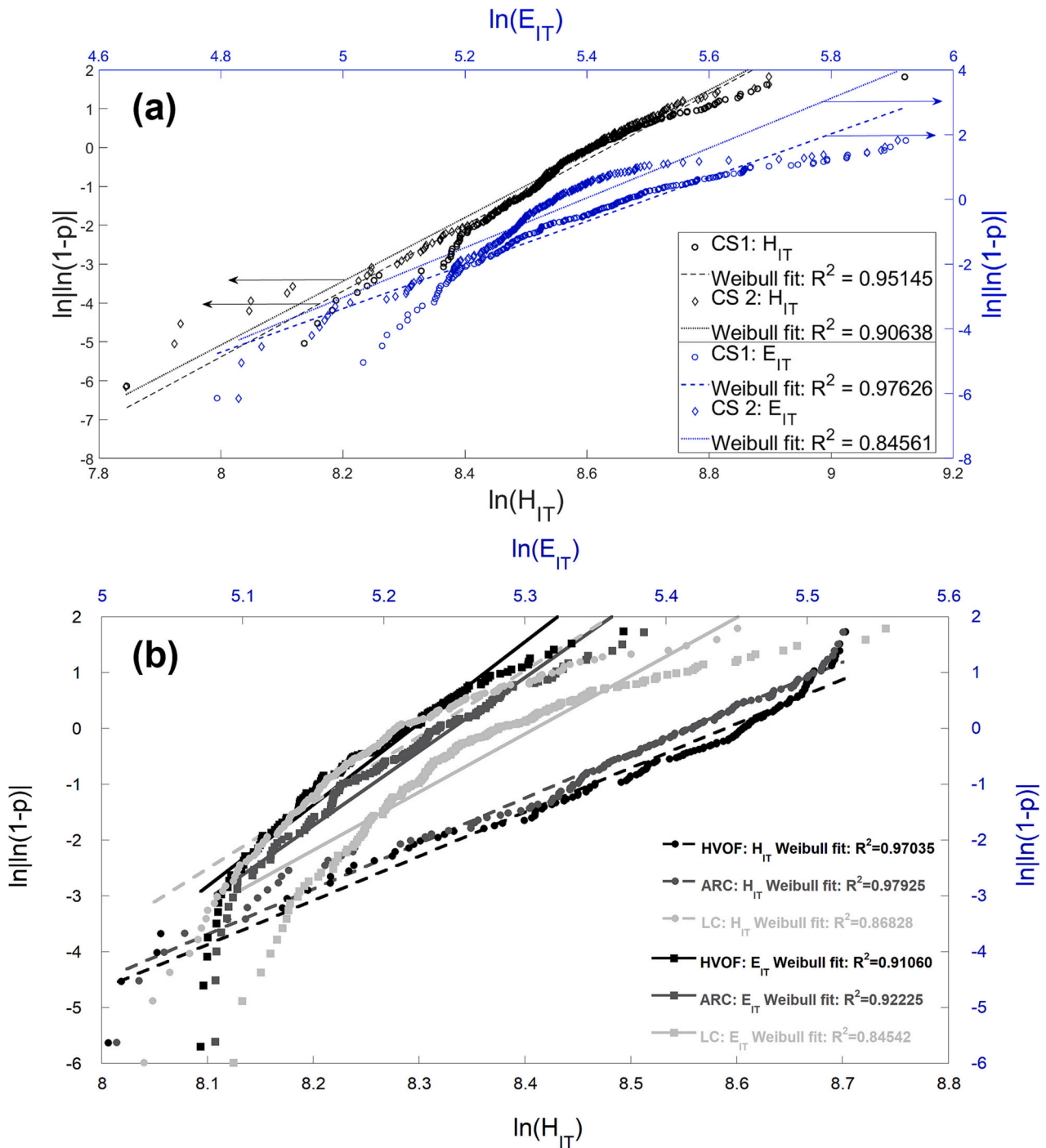

Fig. 9. Weibull plot of the indentation hardness (H_{IT}) and indentation modulus (E_{IT}) data obtained by nanoindentation with corresponding linear fits and R^2 values: a) CS 1 and CS 2 samples; b) HVOF, ARC and LC samples.

GPa and 2.6 GPa were reported for the LC coatings' hardness. The hardness values shown in Fig. 8 are within this reported range.

According to Fig. 8, the HVOF technique provided the highest hardness among the conventional thermally sprayed ones. Chen et al. [47] sprayed Inconel 625 on a 5-mm thick 304 L stainless steel substrate by flame, ARC, plasma, and HVOF spray techniques. They measured the hardness of the coatings through nanoindentation tests using a depth-sensing MTS Nano Indenter XPW with a Berkovich-type pyramidal diamond tip and continuous stiffness measurement methodology. They reported a value of 4.9 GPa and 6.6 GPa for the coatings processed by ARC spraying and HVOF, respectively. They justified the higher hardness values of the HVOF-sprayed sample through the severe plastic deformation of the splats during the deposition process. These hardness values are significantly higher than those obtained in our work (Fig. 8). However, the relative ranking between HVOF and ARC coatings was similar. It must be taken into account that the hardness measurements are affected by the scale of the test, increasing the hardness measured as the indentation size is reduced. The size of the nanoindentations performed by Chen et al. is significantly smaller than the size of the microindentations performed in this work [46].

To investigate the mechanical properties of the CS coatings in more detail, nanoindentation tests were additionally carried out as described in the Materials and Methods section. At a low load of 10 mN, the maximum depth is around 200–215 nm; therefore, the indents are small enough that the associated elastic and (even more) plastic deformation fields fall within a single particle. Thus, the nanoindentation test mostly returns the properties of the material at the intra-particle level, unlike the micro-indentation tests, where indents of a much larger size affect a wider volume of material, encompassing several particles, their interfaces, as well as inter-particle pores and defects. In fact, the micro-hardness values of the CS coatings shown in Fig. 8 correspond to an indentation diagonal of approximately 20 μm, which is comparable to or larger than the size of the primary particles (Table 1). Because the plastically deformed region extends to an even larger region, it is clear that the microindentation data reflects the response of more than one particle, thus encompassing the effect of their interfaces as well.

To verify that the nanoindentation results mainly reflect the properties at the intra-particle level, a Weibull plot of the cumulative probability of indentation hardness, H_{IT}, and elastic modulus, E_{IT}, values are shown in Fig. 9. Indeed, the Weibull distribution is usually regarded as the most appropriate to describe the hardness distribution of thermal spray coatings [48–50]. If the tested material is homogeneous, data can be expected to follow a single Weibull distribution, thus returning a linear Weibull plot [50]. On the other hand, multiple slopes reflecting the co-existence of several Weibull distributions are expected if mechanically different regions exist (as would be the case if there were two or more microstructurally and mechanically distinct areas in the coatings [51], which could also be represented by particles' interiors and weak inter-particle boundaries or pores [52]).

The plot in Fig. 9a shows that the values of CS coatings tend to follow a single linear distribution: linear fits to each data set usually return R^2 values above 0.9; and usually only a limited number of outliers exist at the extremes of each distribution. This result corroborates the initial assumption that nanoindentations reflect intra-particle properties and are scarcely affected by weak boundaries and pores. Because indents were randomly distributed across the section of the coatings, it can also be assumed that in fact there were only few weak interparticle boundaries in the samples. Fig. 9b shows the Weibull distribution for HVOF, ARC and LC coatings. As in the CS samples, the linear fits for the HVOF and ARC samples yielded R^2 values >0.9, and only a limited number of atypical values have been obtained at the extremes of each distribution. Consequently, this result revealed a quasi-homogeneous response of these coatings, indicating a homogeneous microstructure inside the splats, corroborating the microstructure studies reported by Fantozzi et al. [37]. However, the distribution showed by the LC samples is characteristic of a slightly less homogeneous microstructure, with R^2

values close to 0.9. This result agrees with the columnar dendritic with secondary phases observed by Verdi et al. [8] for these coatings.

It is therefore appropriate to treat each data set as a single distribution. Table 2 shows the elastic modulus, E_{IT}, and the nanohardness, H_{IT}, obtained from the nanoindentation tests carried out onto CS (CS 1 and CS 2), HVOF, ARC and LC coatings.

Of all the spraying techniques analysed in this work, the main focus is on cold spraying which has the unique characteristic of being carried out in the solid-state. Therefore, whilst we employed microindentation to test the hardness of all samples, including HVOF, ARC and LC samples employed as references, we decided to deepen the analysis through nanoindentation. The results obtained from HVOF, ARC and LC samples were used as reference; while for CS samples, we wanted to check the intra-particle properties to verify the extent of work-hardening, and to verify the interparticle cohesion through the comparison between nano- and micro-hardness. In fact, at a low load of 10 mN, the maximum depth is around 200–215 nm; therefore, the indents are small enough that the associated elastic and (even more) plastic deformation fields fall within a single particle. Thus, the nanoindentation test mostly returns the properties of the material at the intra-particle level, unlike the micro-indentation tests, where indents of much larger size affect a wider volume of material, encompassing several particles, their interfaces, as well as inter-particle pores and defects. Whilst it is already known that, in conventional thermal spray coatings (e.g. by HVOF and, even more, ARC) the interlamellar cohesion is always somewhat of a weak link, it was interesting to check whether this is true also for the cold sprayed samples. The comparison between the results in Fig. 8 and Table 2 suggests that this is not much the case as the decrease in hardness from nano to micro level because of lamellar boundaries is limited.

The E_{IT} values of the two CS samples, respectively equal to 228 ± 43 GPa and 207 ± 34 GPa, are very similar given the associated error ranges, and they are consistent with the elastic modulus of bulk Inconel 625 which is reported as 207 GPa [53]. Again, this corroborates the above assumption that the nanoindentation tests return "intrinsic" properties at the intra-particle level. Indeed, the elastic modulus of a material depends mostly on its chemical composition and is neither affected by its microstructure nor its work-hardening condition. Therefore, the elastic modulus of the particles is expected not to differ from that of bulk Inconel 625, whatever the degree of work-hardening. However, the other coatings showed values significantly lower than the nominal one. Probably, this result was a consequence of the effect of the weakness in the interlaminar cohesion characteristic of conventional thermal spraying techniques and that could affect the force-displacement curves acting as defects, resulting in a less rigid material.

Interestingly, even the H_{IT} values obtained by nanoindentation (Table 2) are only slightly higher than the microhardness of the corresponding coatings (Fig. 8). A scale-effect is usually expected in the hardness response of thermal spray coatings [54]. As a growing extension of lamellar interfaces is affected by indents at increasingly high loads, there is a correspondingly higher chance that such interfaces surrender during indenter penetration, allowing for inelastic deformation and resulting in a lower measured hardness. The low drop observed in this case is thus another indication of strong inter-particle bonding. In the case of CS coatings, it is consistent with the previous detection of jetting along particle boundaries (Fig. 6) and the correspondingly tight boundaries (Fig. 7).

Table 2
Nanoindentation results for the CS coatings.

Sample	H_{IT} [GPa]	E_{IT} [GPa]
CS 1	5.32 ± 0.77	228 ± 43
CS 2	5.22 ± 0.74	207 ± 34
HVOF	5.05 ± 0.73	180 ± 11
ARC	4.90 ± 0.70	185 ± 12
LC	3.90 ± 0.40	194 ± 17

3.3. Local wear behaviour

Microscratch tests allowed us to measure the local wear behaviour of the coatings. The displaced volume was estimated through Eq. (1). Then, the local wear rate was determined using Eq. (2). Fig. 10 shows SEM images of representative microscratch grooves obtained on the top surface coatings processed by the different spraying techniques.

Common morphological characteristics of the residual grooves generated onto the coatings processed by the different techniques can be identified. Plastically strained material was accumulated along the borders of the residual grooves (details of Fig. 10f, g, h, i), revealing a microploughing mechanism of wear during the microscratch tests. This phenomenon is characterized by the material piling up on the sides of the microscratch grooves [9]. In these images, both the grooves and the side ridges were constant in size for the coatings tested in this work. Then, the wear process may be stationary and also the predominant wear mechanisms [55]. Additionally, the material accumulated in front of the indenter that is not part of the pile-ups is removed by other mechanisms such as microcutting. The morphological characteristics of the residual grooves on the LC coatings generated by scratch have been previously investigated and described by Verdi et al. [8,9], reporting a combination of two wear mechanisms: microploughing and micro-cutting (Fig. 10j). The LC residual grooves showed a limited presence of piling-up material on the sides of the scratch tracks, pointing to the presence of reduced plastic deformation. Consequently, the micro-cutting mechanism contribution is required to justify their wear rates. The microscratch grooves corresponding to the coatings processed by ARC and HVOF also exhibit some cracks revealing an additional mechanism of wear characterized by microcracking (Fig. 10h, i). These cracks appear to follow interparticle boundaries and/or oxide inclusions, thus highlighting the detrimental role of these features for the tribological response of the corresponding coatings.

According to Fig. 10, the aspect ratio of the residual grooves was similar for the coatings tested in this work. Consequently, the higher the residual depth of the scratch tests, the higher the wear rates. Fig. 11 shows representative cross profiles of the scratch tests for the coatings
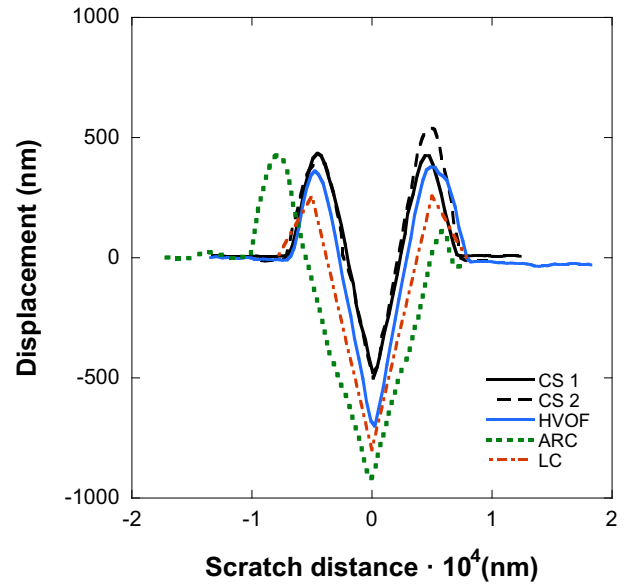

Fig. 11. Representative microscratch tests cross profiles by the different techniques.
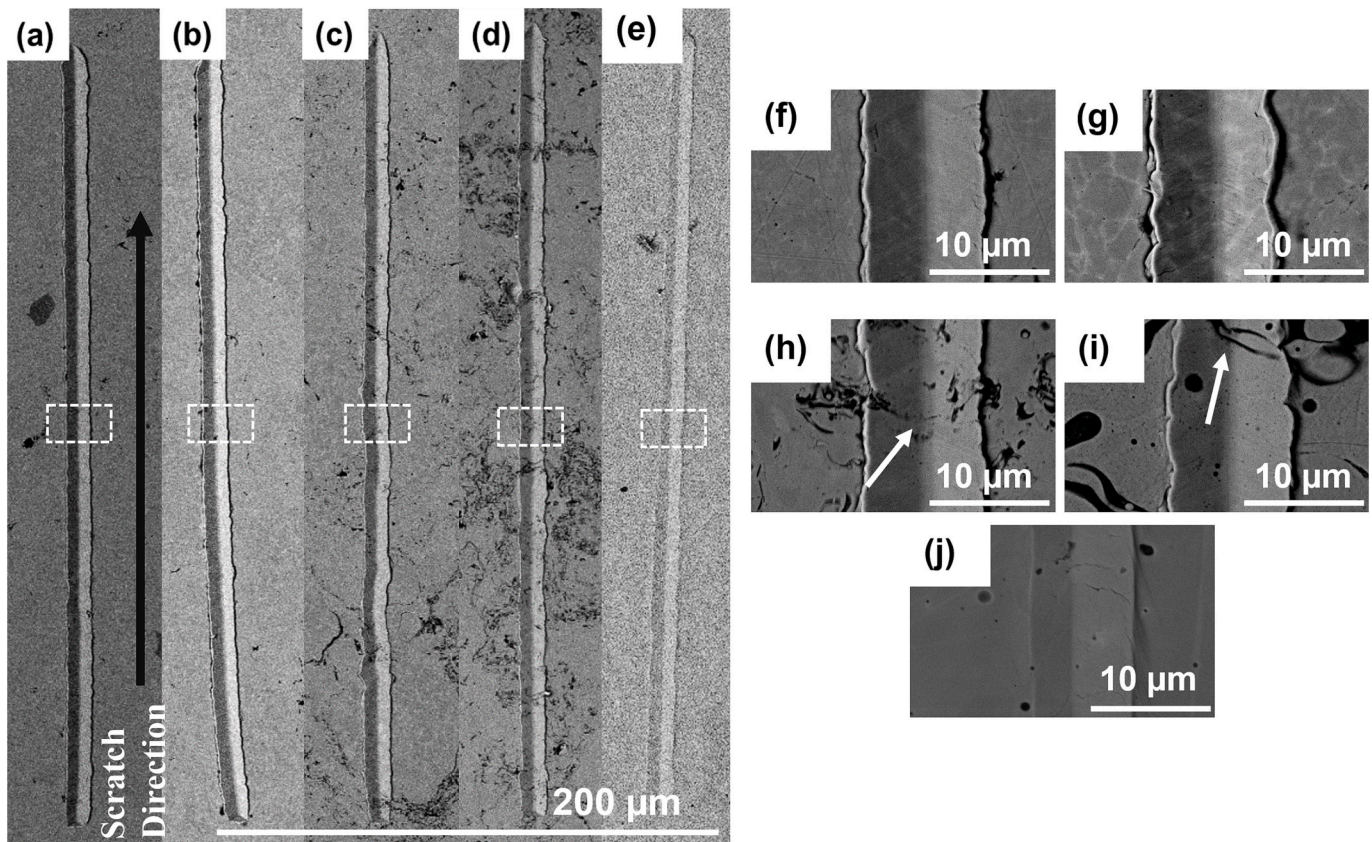LC coatings cross profile data extracted from [57].

Fig. 10. SE Images of microscratch grooves: a) CS 1 (powder $-25 + 5$ μm); b) CS 2 (powder $-38 + 15$ μm); c); HVOF coating; d) ARC sprayed coating; e) LC coating. f), g), h), i) and j) high magnification images from the squared regions in a), b), c), d) and e).

tested in this work. The ARC sprayed coatings showed the higher residual depth with a value of 950 nm. Conversely, CS coatings revealed the lower ones. Therefore, the local wear rates (Fig. 12) were consistent with the depths of the residual grooves (Fig. 11), revealing a relationship between both. Additionally, the highest depth of the scratch grooves was ten times lower than the coatings' thickness. Therefore, no influence of the substrate was expected [56].

Fig. 12 shows the dimensional local wear rates determined from Eq. (2). All values were higher than 10^{-3} mm$^3 \cdot$(N·m)$^{-1}$, as commented below. CS coatings showed the lowest wear rates. Conversely, ARC and LC coatings exhibited the highest wear rates, which were related to their low hardness compared to CS and HVOF coatings. As mentioned above, microploughing and microcutting mechanisms were identified onto CS coatings, whereas the wear grooves on the HVOF and ARC coatings may also be affected by an additional mechanism, microcracking (Fig. 10g and h). This may generate a synergistic effect with the other mechanisms and increase the overall wear rate. Additionally, despite showing similar wear mechanisms to those observed for the CS coatings, the LC coatings exhibited higher wear rates (Fig. 12). This result may reveal the contribution of mechanical properties, such as hardness and the wear behaviour.

Fig. 12 shows the relation between dimensional local wear rate, k, and hardness, H$_v$, for the different techniques. The comparison showed that, generally, the hardness was inversely proportional to k. Namely, coatings with the highest hardness values showed the lowest dimensional local wear rates. This tendency is characteristic of wear dominated by plastic deformation [58]. Therefore, both wear mechanisms identified on the residual scratch grooves, i.e., microploughing and microcutting, were governed by the plastic deformation.

However, the microcracking mechanism observed on HVOF and ARC coatings may have had some influence on the wear process, enhancing the effect of wear on HVOF and ARC coatings. This was particularly apparent for the ARC coating, which showed a higher average wear rate than the LC one despite its higher hardness (Fig. 12). This was likely a consequence of the additional contribution of brittle fracture to the dimensional wear rate of the ARC coating, as will be discussed later.

Conversely, the CS coatings showed the lowest k values with the highest values of hardness, confirming that the plastic deformation and tight inter-particle boundaries resulting from the solid-state deposition process had a particularly favourable effect on the abrasive wear resistance of these samples. This result revealed that the lower the ductility of the coating, the lower the wear rate, thus validating the assumption that the wear process of the coatings was dominated by plastic deformation. A similar conclusion was previously reported by Cavaliere et al. [27] for Inconel 625 CS coatings. Additionally, no significant effect of the grain size was observed.

From the cross profiles of the residual scratch grooves (Fig. 2b), it is possible to estimate the contribution of each of the wear mechanisms that were identified through the analysis of SEM images. The ploughing contribution may be estimated from the V_p/V_d ratio. The material removal contribution due to microcutting and/or microcracking may be evaluated from $(V_d - V_p)/V_d$ relationship.

The results are shown in Fig. 13. In the LC and ARC coatings, the removal mechanisms are dominant with respect to the ploughing one. Consequently, the ability of both coatings to accommodate the displaced material on the groove edges may be limited. It should be noted that this method cannot differentiate between ductile removal (cutting) and brittle cracking. It is likely that brittle cracking contributed somewhat to the material removal from the ARC coating, whilst the LC coating was probably affected almost exclusively by cutting. By contrast, the CS coatings exhibited better ability to accommodate material displaced above the edges of the scratch groove, increasing the size of the pile-ups and making ploughing the dominant wear mechanism. This may be particularly advantageous for wear resistance because ploughed material is removed from the surface more slowly, through plastic fatigue upon repeated abrasive grooving [59].

The type and contribution of each wear mechanism activated during the scratch test could be affected by the microstructure of the coating. Thus, as shown in Fig. 10, CS coatings were characterized by a
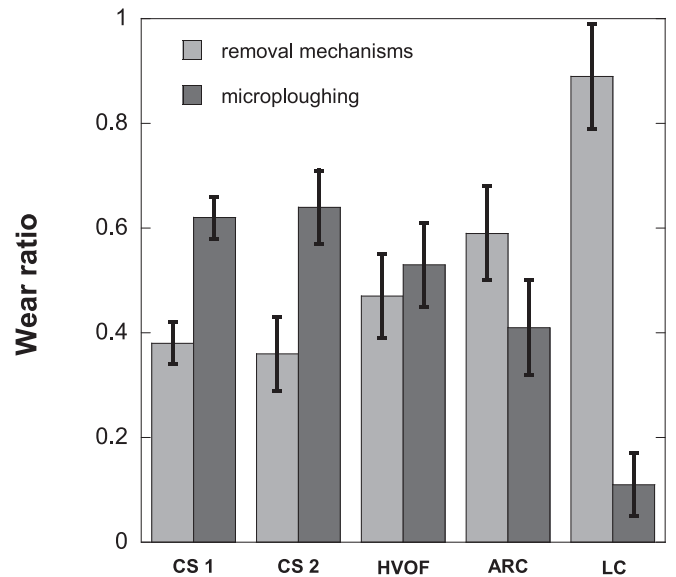

Fig. 13. Wear mechanisms contributions for each coating activated during the scratch process.
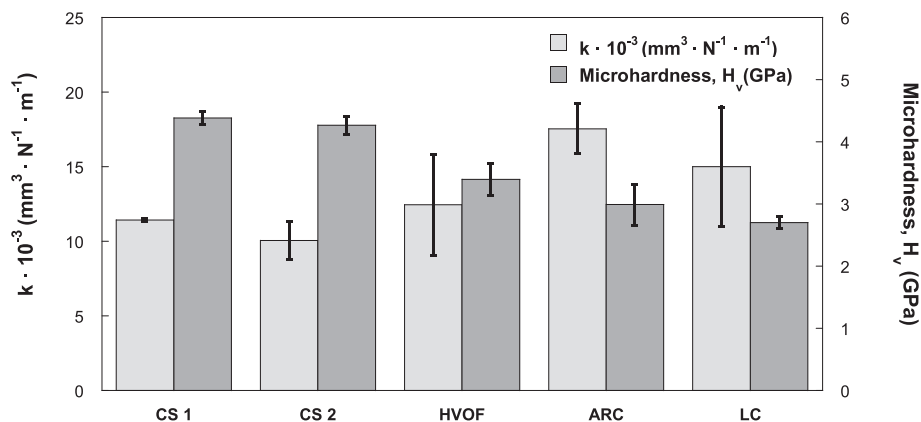

Fig. 12. Relation between wear rate and microhardness from the different techniques. LC coatings data from [9,57].

continuous morphology with no splat boundaries observed. This microstructure could justify an easier development of the ploughing wear mechanism, as compared with cutting, in the CS material. However, HVOF and ARC coatings present a morphology characterized by a high percentage of defects, which may explain a lower tolerance to plastic deformation and a higher contribution of the cutting mechanism in the wear process than that observed for CS coatings. Moreover, this lack of continuity could have favoured the formation of cracks during the scratch process.

To corroborate the above assumptions on wear mechanisms, it is useful to analyse the dimensionless wear coefficient which is related to the dimensional one through H_v, according to the following expression [9]:

$$K = k \cdot H_v \qquad (3)$$

where K is the dimensionless wear coefficient, and it is a measure of the likelihood that an asperity contact leads to material removal. The K value will depend on the mechanisms that are activated during the wear process [60].

Fig. 14 shows the dimensionless local wear coefficient of the coatings deposited by the different techniques. All the coatings showed values $>40 \cdot 10^{-3}$, revealing a wear mechanism clearly dominated by abrasion [61]. Consequently, the mechanical displacement of the material by the action of the indenter sliding across the coatings′surfaces was developed by an abrasive grooving wear mode. The ARC coatings showed greater average dimensionless wear coefficients, probably because grooving occurs by brittle fracture in addition to ductile grooving mechanisms (ploughing or cutting). This corroborates the previous considerations. By contrast, the lowest average dimensionless wear coefficient was obtained with the LC coating. Although the widths of the associated error bars make it difficult to differentiate the LC and CS samples, this result reflects the near-complete absence of any brittle fracture phenomena on the LC sample, due to the high cohesion of its microstructure. This cohesion is at least as good as that of the CS samples. Consequently, the greater wear loss of the LC coating is not due to the onset of brittle wear mechanisms, consistent with the hypotheses put forward previously. Grooving occurs by ductile mechanisms in both LC and CS samples. However, due to the lower hardness of the LC coating, each ductile grooving event leads to the displacement of a larger volume of material (probably by cutting, when this result is coupled to the fraction of material removal in Fig. 13) than it does on the harder CS samples.
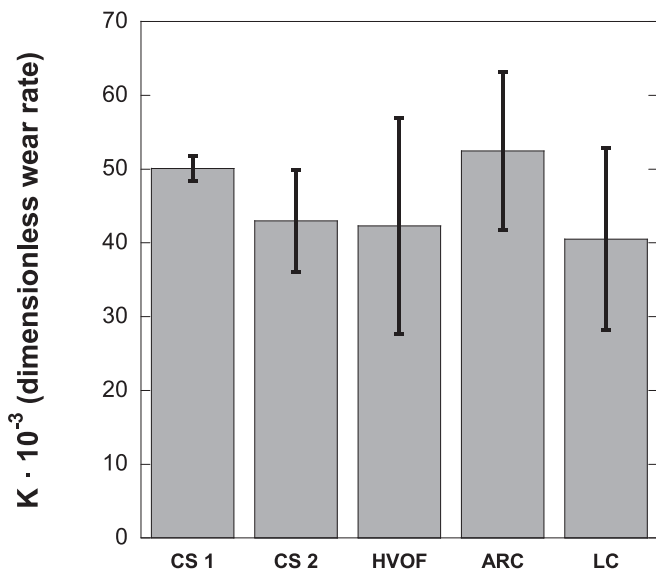
Notably, it appears that the HVOF sample also exhibits approximately the same dimensionless wear coefficient as the CS and LC samples, despite the visible occurrence of microcracking in Fig. 10g. Therefore, it is inferred that microcracking phenomena are not especially influential on the overall displacement and loss of material from the HVOF coating. Rather, this is more affected by the lower hardness of this coating, compared to the CS ones, likely due to oxide inclusions and interlamellar defects weakening the overall cohesion. Thus, the slightly higher contribution of removal rather than ploughing mechanisms in the HVOF sample (Fig. 13) can also be ascribed to cutting (like for the LC coating) rather than brittle fracture.

It is worth highlighting the high values of wear rates obtained from a microscratch test compared to those reported from dry sliding wear tests. Wear rate values with orders of magnitude of 10^{-5} and 10^{-4} $mm^3 \cdot N^{-1} \cdot m^{-1}$ are common in dry sliding wear tests. Gao et al. [62] reported values of $1 \cdot 10^{-5}$ $mm^3 \cdot N^{-1} \cdot m^{-1}$ for untreated bulk Inconel 625 under a ball-on-disc sliding wear test configuration. Similarly, Wu et al. [29] studied the tribological properties of 625 coatings deposited on 6061 aluminum alloy using a high-pressure cold spray process. They carried out dry sliding wear tests at room temperature on Inconel 625 coatings through a ball-on-disc arrangement. They reported values of the specific wear rates that ranged between $10 \cdot 10^{-5}$ to $40 \cdot 10^{-5}$ $mm^3 \cdot N^{-1} \cdot m^{-1}$ depending on the sliding velocity. Srichen et al. [63] also employed the ball-on-disc test to study the influence of heat treatments on the tribological behaviour of ARC NiCrMoAl alloy coatings at room temperature. For the as-sprayed coatings, they reported a specific wear rate of $4 \cdot 10^{-5}$ $mm^3 \cdot N^{-1} \cdot m^{-1}$. These wear rates values are significantly lower than that obtained from microscratch tests in the present work (Fig. 10). This discrepancy may have occurred, on the one hand, because in the microscratch tests the formation of the mechanically mixed layers, the occurrence of tribo-oxidation and wear of the counterbody asperities are limited. All these phenomena can limit the wear loss of the coating. Moreover, in the present tests, the calculation of the specific wear rate according to Eqs. (1) and (2) included both the fraction of material that was plastically displaced without removal and the fraction of removed material. In ball-on-disc tests, by contrast, the specific wear rate is usually calculated only using the volume of removed material. If we consider only the fraction of removed material according to Fig. 13, the specific wear rates of the CS samples decrease to around $4 \cdot 10^{-4}$ $mm^3 \cdot N^{-1} \cdot m^{-1}$, which are closer to the upper limit of the range of specific wear rates reported in the literature. This also reflects the contribution due to "pure" abrasive grooving, with no tribochemical/tribo-oxidative contributions (e.g., mechanically mixed layers' formation and/or tribo-oxidation, as mentioned above). Accordingly, the difference between single microscratch experiments and full ball-on-disc tests may give a clear sign of the relevance of tribochemical phenomena in mitigating the sliding wear loss against hard counterparts. Interestingly, the large contribution of removal mechanisms (mostly cutting, based on the earlier considerations) to the specific wear rate of the LC sample means that its "removal-only" specific wear rate is still close to the value listed in Fig. 12, i.e., above 10^{-3} $mm^3 \cdot N^{-1} \cdot m^{-1}$. This underlines how the low hardness of the coarser and more diluted LC coating might be especially detrimental to the wear resistance.

4. Conclusions

Inconel 625 coatings processed by CS, using two powder size distributions, and by several conventional techniques, including HVOF, ARC and LC, were analysed. Microstructure, Vickers hardness, nano-hardness and local wear behaviour were evaluated, leading to the following conclusions.

- No oxides were observed in the CS coatings due to the low deposition temperatures by SEM. CS coatings exhibit a plastically deformed dendritic microstructure affected by the powder size distribution. Finer powders originally contained a finer dendritic microstructure

Fig. 14. Dimensionless wear coefficient of coating deposited by different techniques.

(which is retained in the CS coating) and undergo more extensive and uniform plastic deformation upon impact.

- CS materials exhibit the greatest hardness due to the plastic deformation developed during deposition. No significant effects of powder size distribution were detected. The lowest hardness was measured in the ARC coating, due to limited interlamellar cohesion and extensive oxidation, and the LC coating, due to dilution processes during deposition.
- The main wear mechanism observed in all the deposited materials was ductile grooving which could be specifically differentiated into two sub-mechanisms: microploughing and microcutting. However, ARC and HVOF coatings also exhibited microcracking. Especially in the ARC coating, the latter wear mechanism is combined with plastic grooving in a synergistic manner, increasing the local wear rate.
- CS materials exhibited the highest wear resistance and no clear effect from the particle size distribution was detected. HVOF and LC samples, despite exhibiting a similar tendency to ductile and brittle grooving, suffered higher specific wear rates due to the lower hardness. This also implied a greater tendency toward microcutting (with direct removal of material) rather than microploughing (with no material removal). Thus, when specific wear rates are calculated based only on the removed fraction of material (i.e., excluding the fraction of plastically displaced material), there is an even larger difference between CS coatings, on the one hand, and LC and HVOF coatings, on the other.
- The microscratch test allows obtaining wear rates not affected by other phenomena that depend on the wear test configuration, such as tribo-oxidation or mechanically mixed layers. Thus, specific wear rates under microscratch conditions are usually higher than in a sliding wear test involving multiple contact events, like a ball-on-disc test, and allow characterizing a purely "mechanical" response from the material.

Therefore, from this work it can be concluded that the main wear mechanism observed in all the deposited materials was ductile grooving, regardless of the thermal spraying technique. The ductile character of the metallic alloy dominates over the spraying technique. Consequently, the analysis of the wear rates allows to conclude that the coatings deposited by CS are those with the highest scratch wear resistance. This result is directly related to a higher hardness exhibited by these coatings. Finally, this behaviour seems to be independent of the powder size used in the manufacturing process of the CS coatings, at least in the range studied in this work.

CRediT authorship contribution statement

Rocío Cortés: Methodology, Validation, Formal analysis, Investigation, Writing – review & editing. **Miguel Ángel Garrido-Maneiro:** Conceptualization, Methodology, Validation, Formal analysis, Investigation, Writing – original draft, Writing – review & editing. **Heli Koivuluoto:** Methodology, Validation, Investigation, Resources. **Giovanni Bolelli:** Methodology, Validation, Investigation, Formal analysis, Writing – original draft, Writing – review & editing. **Stefania Morelli:** Methodology, Validation, Formal analysis, Investigation. **Veronica Testa:** Validation, Formal analysis, Investigation. **Luca Lusvarghi:** Methodology, Validation, Formal analysis, Investigation, Writing – original draft, Writing – review & editing. **Jan Kondas:** Methodology, Validation, Investigation, Resources. **Pedro Poza:** Conceptualization, Methodology, Writing – original draft, Writing – review & editing, Supervision.

Declaration of competing interest

The authors declare that they have no known competing financial interests or personal relationships that could have appeared to influence the work reported in this paper.

Data availability

No data was used for the research described in the article.

References

[1] F.J. Xu, Y.H. Lv, B.S. Xu, Y.X. Liu, F.Y. Shu, P. He, Effect of deposition strategy on the microstructure and mechanical properties of Inconel 625 superalloy fabricated by pulsed plasma arc deposition, Mater. Des. 45 (2013) 446–455, https://doi.org/10.1016/J.MATDES.2012.07.013.

[2] H.N. Moosavy, M.R. Aboutalebi, S.H. Seyedein, An analytical algorithm to predict weldability of precipitation-strengthened nickel-base superalloys, J. Mater. Process. Technol. 212 (2012) 2210–2218, https://doi.org/10.1016/J.JMATPROTEC.2012.06.010.

[3] T. Baidridge, G. Poling, E. Foroozmehr, R. Kovacevic, T. Metz, V. Kadekar, M. C. Gupta, Laser cladding of Inconel 690 on Inconel 600 superalloy for corrosion protection in nuclear applications, Opt. Lasers Eng. 51 (2013) 180–184, https://doi.org/10.1016/J.OPTLASENG.2012.08.006.

[4] S. Sampath, X.Y. Jiang, J. Matejicek, L. Prchlik, A. Kulkarni, A. Vaidya, Role of thermal spray processing method on the microstructure, residual stress and properties of coatings: an integrated study for Ni–5 wt.%Al bond coats, Mater. Sci. Eng. A 364 (2004) 216–231, https://doi.org/10.1016/J.MSEA.2003.08.023.

[5] P. Rambabu, N.E. Prasad, V.V. Kutumbarao, R.J.H. Wanhill, Aerospace Materials and Material Technologies, 2016, https://doi.org/10.1007/978-981-10-2134-3.

[6] R. Revie, H. Uhlig, Corrosion and Corrosion Control: An Introduction to Corrosion Science and Engineering, 3rd ed., Wiley, 2008.

[7] N. Ahmed, M.S. Bakare, D.G. McCartney, K.T. Voisey, The effects of microstructural features on the performance gap in corrosion resistance between bulk and HVOF sprayed Inconel 625, Surf. Coat. Technol. 204 (2010) 2294–2301, https://doi.org/10.1016/J.SURFCOAT.2009.12.028.

[8] D. Verdi, M.A. Garrido, C.J. Múnez, P. Poza, Influence of exposure at high temperature on the local scratch mechanisms in laser cladded Inconel 625-base metal matrix composite coatings, J. Alloys Compd. 733 (2018) 69–81, https://doi.org/10.1016/j.jallcom.2017.10.291.

[9] D. Verdi, M.A. Garrido, C.J. Múnez, P. Poza, Cr3C2 incorporation into an Inconel 625 laser cladded coating: effects on matrix microstructure, mechanical properties and local scratch resistance, Mater. Des. 67 (2015) 20–27, https://doi.org/10.1016/j.matdes.2014.10.086.

[10] F. Azarmi, H.R. Salimijazi, Grain growth and pore elimination in Inconel 625 deposited by APS, Surf. Coat. Technol. 268 (2015) 3–6, https://doi.org/10.1016/J.SURFCOAT.2014.08.011.

[11] C. Leither, J. Risan, M. Bashirzadeh, F. Azarmi, Determination of the elastic modulus of wire arc sprayed alloy 625 using experimental, analytical, and numerical simulations, Surf. Coat. Technol. 235 (2013) 611–619, https://doi.org/10.1016/J.SURFCOAT.2013.08.033.

[12] A.A. Boudi, M.S.J. Hashmi, B.S. Yilbas, HVOF coating of Inconel 625 onto stainless and carbon steel surfaces: corrosion and bond testing, J. Mater. Process. Technol. 155–156 (2004) 2051–2055, https://doi.org/10.1016/J.JMATPROTEC.2004.04.146.

[13] F. Azarmi, I. Sevostianov, Comparative micromechanical analysis of alloy 625 coatings deposited by air plasma spraying, wire arc spraying, and cold spraying technologies, Mech. Mater. 144 (2020), 103345, https://doi.org/10.1016/J.MECHMAT.2020.103345.

[14] A. Papyrin, Cold Spray Technology, Elsevier, 2007.

[15] J. Karthikeyan, The advantages and disadvantages of the cold spray coating process, in: The Cold Spray Materials Deposition Process: Fundamentals and Applications, 2007, pp. 62–71, https://doi.org/10.1533/9781845693787.1.62.

[16] J. Villafuerte, Modern Cold Spray: Materials, Process, and Applications, Springer International Publishing, 2015, https://doi.org/10.1007/978-3-319-16772-5.

[17] H. Assadi, H. Kreye, F. Gärtner, T. Klassen, Cold spraying – a materials perspective, Acta Mater. 116 (2016) 382–407, https://doi.org/10.1016/J.ACTAMAT.2016.06.034.

[18] H. Assadi, F. Gärtner, T. Stoltenhoff, H. Kreye, Bonding mechanism in cold gas spraying, Acta Mater. 51 (2003) 4379–4394, https://doi.org/10.1016/S1359-6454(03)00274-X.

[19] P. Poza, M.Á. Garrido-Maneiro, Cold-sprayed coatings: microstructure, mechanical properties, and wear behaviour, Prog. Mater. Sci. 123 (2022), https://doi.org/10.1016/j.pmatsci.2021.100839.

[20] T. Suhonen, T. Varis, S. Dosta, M. Torrell, J.M. Guilemany, Residual stress development in cold sprayed Al, Cu and Ti coatings, Acta Mater. 61 (2013) 6329–6337, https://doi.org/10.1016/J.ACTAMAT.2013.06.033.

[21] C.A. Widener, O.C. Ozdemir, M. Carter, Structural repair using cold spray technology for enhanced sustainability of high value assets, Procedia Manuf. 21 (2018) 361–368, https://doi.org/10.1016/J.PROMFG.2018.02.132.

[22] K. Petráčková, J. Kondás, M. Guagliano, Fixing a hole (with cold spray), Int. J. Fatigue 110 (2018) 144–152, https://doi.org/10.1016/J.IJFATIGUE.2018.01.014.

[23] V.K. Champagne, The Cold Spray Materials Deposition Process: Fundamentals and Applications, Elsevier Ltd, 2007, https://doi.org/10.1533/9781845693787.

[24] T. Schmidt, H. Assadi, F. Gärtner, H. Richter, T. Stoltenhoff, H. Kreye, T. Klassen, From particle acceleration to impact and bonding in cold spraying, J. Therm. Spray Technol. 18 (2009) 794–808, https://doi.org/10.1007/S11666-009-9357-7/FIGURES/22.

[25] H. Assadi, T. Schmidt, H. Richter, J.O. Kliemann, K. Binder, F. Gärtner, T. Klassen, H. Kreye, On parameter selection in cold spraying, J. Therm. Spray Technol. 20 (2011) 1161–1176, https://doi.org/10.1007/S11666-011-9662-9.

[26] A. Pontarollo, S. Vezzù, A. Trentin, S. Rech, M. Guidolin, A. Cafissi, C. Peretti, B. Molinas, Characterisation of Inconel 625 coatings deposited by cold spray - ASM International, in: Thermal Spray 2011: Proceedings from the International Thermal Spray Conference, 2011, pp. 746–750, https://doi.org/10.31399/asm.cp.itsc2011p0746.

[27] P.D. Cavaliere, A. Rizzo, D. Valerini, L. Capodieci, Wear and fretting behavior of cold sprayed IN625 superalloy, in: Metals 2021 11, 2020, p. 49, https://doi.org/10.3390/MET11010049.

[28] A. Chaudhuri, Y. Raghupathy, D. Srinivasan, S. Suwas, C. Srivastava, Microstructural evolution of cold-sprayed Inconel 625 superalloy coatings on low alloy steel substrate, Acta Mater. 129 (2017) 11–25, https://doi.org/10.1016/J.ACTAMAT.2017.02.070.

[29] K. Wu, W. Sun, A.W.Y. Tan, I. Marinescu, E. Liu, W. Zhou, An investigation into microstructure, tribological and mechanical properties of cold sprayed Inconel 625 coatings, Surf. Coat. Technol. 424 (2021), 127660, https://doi.org/10.1016/J.SURFCOAT.2021.127660.

[30] E.O. Ezugwu, Z.M. Wang, A.R. Machado, The machinability of nickel-based alloys: a review, J. Mater. Process. Technol. 86 (1999) 1–16, https://doi.org/10.1016/S0924-0136(98)00314-8.

[31] X. Chen, J.W. Hutchinson, Particle impact on metal substrates with application to foreign object damage to aircraft engines, J. Mech. Phys. Solids 50 (2002) 2669–2690, https://doi.org/10.1016/S0022-5096(02)00022-4.

[32] M. Shakil, M. Ahmad, N.H. Tariq, B.A. Hasan, J.I. Akhter, E. Ahmed, M. Mehmood, M.A. Choudhry, M. Iqbal, Microstructure and hardness studies of electron beam welded Inconel 625 and stainless steel 304L, Vacuum. 110 (2014) 121–126, https://doi.org/10.1016/J.VACUUM.2014.08.016.

[33] K. Krishnaveni, T.S.N. Sankara Narayanan, S.K. Seshadri, Electroless Ni–B coatings: preparation and evaluation of hardness and wear resistance, Surf. Coat. Technol. 190 (2005) 115–121, https://doi.org/10.1016/j.surfcoat.2004.01.038.

[34] G. Pintaude, F.G. Bernardes, M.M. Santos, A. Sinatora, E. Albertin, Mild and severe wear of steels and cast irons in sliding abrasion, Wear. 267 (2009) 19–25, https://doi.org/10.1016/J.WEAR.2008.12.099.

[35] Y. Wang, S. Zhao, Z. Jia, J. Ji, D. Liu, T. Guo, Y. Ding, Study on friction and wear behavior of Inconel 625 superalloy during hot extrusion, Adv. Mater. Sci. Eng. 2020 (2020), https://doi.org/10.1155/2020/5453703.

[36] M.J. Cieslak, T.J. Headley, A.D. Romig, T. Kollie, M.J. Cieslak, T.J. Headley, A. D. Romig, T. Kollie, A melting and solidification study of alloy 625, MTA. 19 (1988) 2319–2331, https://doi.org/10.1007/BF02645056.

[37] D. Fantozzi, V. Matikainen, M. Uusitalo, H. Koivuluoto, P. Vuoristo, Chlorine-induced high temperature corrosion of Inconel 625 sprayed coatings deposited with different thermal spray techniques, Surf. Coat. Technol. 318 (2017) 233–243, https://doi.org/10.1016/J.SURFCOAT.2016.12.086.

[38] AENOR, UNE-EN ISO 6507-1:2018 Materiales metálicos. Ensayo de dureza, 2018.

[39] G. Mauer, R. Singh, K.H. Rauwald, S. Schrüfer, S. Wilson, R. Vaßen, Diagnostics of cold-sprayed particle velocities approaching critical deposition conditions, J. Therm. Spray Technol. 26 (2017) 1423–1433, https://doi.org/10.1007/S11666-017-0596-8/FIGURES/10.

[40] S. Adachi, N. Ueda, Effect of cold-spray conditions using a nitrogen propellant gas on AISI 316L stainless steel-coating microstructures, Coatings. 7 (2017), https://doi.org/10.3390/coatings7070087.

[41] C.W. Kang, H.W. Ng, S.C.M. Yu, Imaging diagnostics study on obliquely impacting plasma-sprayed particles near to the substrate, J. Therm. Spray Technol. 15 (2006) 118–130, https://doi.org/10.1361/105996306X92686/METRICS.

[42] D. Poirier, Y. Thomas, B. Guerreiro, M. Martin, M. Aghasibeig, E. Irissou, Improvement of tool steel powder cold sprayability via softening and agglomeration heat treatments, J. Therm. Spray Technol. 31 (2022) 145, https://doi.org/10.1007/S11666-022-01320-4.

[43] C. Borchers, T. Schmidt, F. Gärtner, H. Kreye, High strain rate deformation microstructures of stainless steel 316L by cold spraying and explosive powder compaction, Appl. Phys. A 90 (3) (2007) 517–526, https://doi.org/10.1007/S00339-007-4314-0.

[44] T.Y. Yung, T.C. Chen, K.C. Tsai, W.F. Lu, J.Y. Huang, T.Y. Liu, Thermal spray coatings of Al, ZnAl and Inconel 625 alloys on SS304L for anti-saline corrosion, Coatings 9 (2019) 32, https://doi.org/10.3390/COATINGS9010032.

[45] V.R.S. Sá Brito, I.N. Bastos, H.R.M. Costa, Corrosion resistance and characterization of metallic coatings deposited by thermal spray on carbon steel, Mater. Des. 41 (2012) 282–288, https://doi.org/10.1016/J.MATDES.2012.05.008.

[46] K. Feng, Y. Chen, P. Deng, Y. Li, H. Zhao, F. Lu, R. Li, J. Huang, Z. Li, Improved high-temperature hardness and wear resistance of Inconel 625 coatings fabricated by laser cladding, J. Mater. Process. Technol. 243 (2017) 82–91, https://doi.org/10.1016/J.JMATPROTEC.2016.12.001.

[47] T.C. Chen, C.C. Chou, T.Y. Yung, R.F. Cai, J.Y. Huang, Y.C. Yang, A comparative study on the tribological behavior of various thermally sprayed Inconel 625 coatings in a saline solution and deionized water, Surf. Coat. Technol. 385 (2020), 125442, https://doi.org/10.1016/J.SURFCOAT.2020.125442.

[48] T. Valente, Statistical evaluation of Vicker's indentation test results for thermally sprayed materials, Surf. Coat. Technol. 90 (1997) 14–20, https://doi.org/10.1016/S0257-8972(96)03077-0.

[49] R.S. Lima, B.R. Marple, High Weibull modulus HVOF titania coatings, J. Therm. Spray Technol. 12 (2003) 240–249, https://doi.org/10.1361/105996303770348357/METRICS.

[50] P. Suresh Babu, D. Srinivasa Rao, L. Rama Krishna, G. Sundararajan, Weibull analysis of hardness distribution in detonation sprayed nano-structured WC-12Co coatings, Surf. Coat. Technol. 319 (2017) 394–402, https://doi.org/10.1016/J.SURFCOAT.2017.04.028.

[51] P. Fauchais, G. Montavon, R.S. Lima, B.R. Marple, Engineering a new class of thermal spray nano-based microstructures from agglomerated nanostructured particles, suspensions and solutions: an invited review, J. Phys. D. Appl. Phys. 44 (2011), 093001, https://doi.org/10.1088/0022-3727/44/9/093001.

[52] G. Bolelli, M.G. Righi, M.Z. Mughal, R. Moscatelli, O. Ligabue, N. Antolotti, M. Sebastiani, L. Lusvarghi, E. Bemporad, Damage progression in thermal barrier coating systems during thermal cycling: a nano-mechanical assessment, Mater. Des. 166 (2019), 107615, https://doi.org/10.1016/J.MATDES.2019.107615.

[53] W.D. Callister, D.G. Rethwisch, Materials Science and Engineering an Introduction With Special Contributions by, 2007.

[54] J. Nohava, B. Bonferroni, G. Bolelli, L. Lusvarghi, Interesting aspects of indentation and scratch methods for characterization of thermally-sprayed coatings, Surf. Coat. Technol. 205 (2017) 1127–1131, https://doi.org/10.1016/J.SURFCOAT.2010.08.086.

[55] M.A. Masen, M.B. De Rooij, D.J. Schipper, Micro-contact based modelling of abrasive wear, Wear. 258 (2005) 339–348, https://doi.org/10.1016/J.WEAR.2004.09.009.

[56] ASTM: E10 - 15, Standard Test Method for Brinell Hardness of Metallic Materials 1, 2019, https://doi.org/10.1520/E0010-15.

[57] D. Verdi, Effect of the Temperature on the Microstructure and the Mechanical Properties of Laser Cladded Ni-based Metal Matrix Composite Coatings, University of Rey Juan Carlos, 2015.

[58] I. Hutchings, P. Shipway, Tribology: Friction and Wear of Engineering Materials, Second edition, Elsevier Inc., 2017.

[59] K.H.Z. Gahr, Formation of wear debris by the abrasion of ductile metals, Wear. 74 (1981) 353–373, https://doi.org/10.1016/0043-1648(81)90173-3.

[60] K. Hokkirigawa, K. Kato, An experimental and theoretical investigation of ploughing, cutting and wedge formation during abrasive wear, Tribol. Int. 21 (1988) 51–57, https://doi.org/10.1016/0301-679X(88)90128-4.

[61] A.L. Greer, K.L. Rutherford, I.M. Hutchings, Wear resistance of amorphous alloys and related materials, Int. Mater. Rev. 47 (2013) 87–112, https://doi.org/10.1179/095066001225001067.

[62] Q. L., Y. Gao, X. Li, Y. Ma, M. Kitchen, Y. Ding, Formation mechanism and wear behavior of gradient nanostructured Inconel 625 alloy, Trans. Nonferrous Metals Soc. China 32 (2022) 1910–1925, https://doi.org/10.1016/S1003-6326(22)65918-1.

[63] A. Srichen, S. Moonngam, S. Linjee, C. Banjongprasert, Tribological behaviors of arc sprayed NiCrMoAl alloy coating after heat treatments, Surf. Coat. Technol. 437 (2022), 128325, https://doi.org/10.1016/J.SURFCOAT.2022.128325.